Modulated Polarization Microscopy: A Promising New Approach to Visualizing Cytoskeletal Dynamics in Living Cells

Jeffrey R. Kuhn, Zhuoru Wu, and Martin Poenie
Division of Molecular Cell and Developmental Biology, University of Texas, Austin, Texas 78712 USA

ABSTRACT In an effort to visualize cytoskeletal filaments in living cells, we have developed modulated polarization microscopy. Modulated polarization microscopy visualizes cytoskeletal filaments based on their birefringence but differs from the standard polarization microscopy by exploiting the angle dependence of birefringence. A prototype instrument has been developed using two Faraday rotators under computer control to change the angle of plane polarized light at a known rate. By placing one Faraday rotator before and one after the specimen, rotation produced by the first Faraday rotator is cancelled by the second. This allows the use of fixed polarizer and analyzer in a crossed configuration and continuous imaging of the specimen between crossed polarizers. The variation in polarization angle of light illuminating the specimen causes birefringent elements to oscillate in brightness. Images acquired as polarization angle is varied are then processed by a Fourier filter image-processing algorithm. The Fourier filtering algorithm isolates those signals that vary at the proper rate, whereas static or random signals are removed. Here we show that the modulated polarization microscope can reveal cytoskeletal elements including stress fibers and microtubules in living cells.

INTRODUCTION

Cells use systems of filaments, collectively referred to as the cytoskeleton, to establish and maintain their shape and to generate various types of cell movements. Until recently, visualization of cytoskeletal filaments was mainly limited to immunofluorescent staining of fixed cells or fluorescent analog cytochemistry for living cells (Wang, 1989). The introduction of green fluorescent protein (GFP) technology has made it possible to visualize cytoskeletal filaments in living cells through the expression of a chimeric fusion protein formed from GFP and the cytoskeletal protein of interest (Gerdes and Kaether, 1996; Prendergast, 1999; Tsien, 1998). Although this technology is a great advance, it suffers from the drawback that some cells such as T lymphocytes are difficult to transfect. Furthermore, we have found that, even when murine T lymphocytes were successfully transfected with GFP-tubulin constructs, the background fluorescence obscured that of individual microtubules.

Alternative approaches for visualizing the cytoskeleton in living cells have been developed based on the interaction of polarized light with birefringent polymers. Although polarized light has been used for decades to visualize the microtubule-dependent birefringence of the mitotic spindle (Cassimeris et al., 1988; Czaban and Forer, 1985; Swann and Mitchison, 1950), it has generally not been useful for seeing the much weaker birefringence of actin bundles or individual microtubules. This is largely due to the relatively high background caused by the depolarization of light at lens surfaces and the scattering of light by components of the cytoplasm (Inoué and Hyde, 1957).

Received for publication 17 May 2000 and in final form 3 November 2000.
Address reprint requests to Martin Poenie, University of Texas–Austin, Department of Zoology, 141 Patterson Labs., Austin, TX 78712-1064. Tel.: 512-471-5598; Fax: 512-471-9651; E-mail: poenie@mail.utexas.edu.

0006-3495/01/02/972/14 $2.00

The sensitivity of polarized light microscopy can be improved through the use of a rectified condenser (Inoué and Hyde, 1957) or by the use of a compensator, together with image-processing techniques for background subtraction (Allen and Allen, 1983; Inoué, 1981). The rectified condenser reduces the background arising from the depolarization of light at lens surfaces. The use of a compensator can improve sensitivity by adding a fixed retardation to that of a weakly birefringent structure. This improves sensitivity by shifting the signal of the birefringent object into the more linear region of the sinusoidal amplitude curve (Allen et al., 1966; Swann and Mitchison, 1950). A compensator also improves the point-spread function to give a better approximation of an Airy disk and thus an improvement in resolution (Hansen, 1988). Unfortunately, none of these improvements has made polarized light microscopy generally useful as a means for imaging the interphase cytoskeleton in living cells. The rectified condenser reduces the background due to the microscope optics but it does not affect the background contributed by the cytoplasm. The compensator provides an increase in the signal of birefringent components but at the expense of a large increase in background. At the optimal compensator setting of 45°, the difference in the amplitude of birefringent signals and the background greatly exceeds the dynamic range of video cameras.

A third approach is to isolate the birefringent signal of cytoskeletal components by some form of ellipsometry. This was first explored by Allen and Nakajima (1965) who described a method of creating two photomicrographs of a specimen at opposite compensator settings. From densitometry measurements on these photographs, they were able to estimate retardances, but these measurements were tedious and time consuming. Faster and more direct instruments were developed using either a tilting mica compensator or a Pockel cell to modulate polarization while simultaneously measuring the variation in amplitude using a photomulti-

plier tube (Allen and Rebhun, 1962). Although the published instrument only sampled a single spot, the authors mentioned future plans to scan the specimen to obtain the birefringence of the entire field.

A scanning imaging ellipsometer similar in principle to that envisioned by Allen was constructed by Baker and Johnston (1967). Here, a spot on the specimen was illuminated by a HeNe laser and polarization was modulated by two Pockel cells, one on each side of the microscope stage. The amplitude of the intensity oscillation was measured by a photomultiplier tube linked to a band-pass filter and displayed on an image storage oscilloscope. By scanning the specimen, they were thus able to record a birefringence image. Unfortunately, the quality of their single published oscilloscope trace "image" was quite poor and Allen (1967) commented saying, "any serious attempt to interpret such an image in molecular terms should be classified as 'inference microscopy.'"

More recently, Oldenbourg (1996) developed a new type of polarization microscope using two variable liquid crystal retarders to modulate the polarization state. In principle, the polarization is set to four different states; left circular, right circular, crossed, and parallel. From this, the four Stokes polarization parameters can be calculated on a pixel-by-pixel basis. In practice, the four polarization states serve as limits that cannot be achieved because of the restricted dynamic range of the camera. Instead, the polarization state is moved in the direction of each of these four limits. Although this method has produced some excellent pictures of cytoskeletal elements, the low polarization purity of liquid crystal retarders limits the sensitivity of the instrument, and their method of modulating the polarization state does not exploit the full amplitude of the birefringent signal.

Here, we present an alternative approach for selectively imaging birefringent objects that we call modulated polarization microscopy (MPM). This method attempts to maintain a high degree of polarization purity by using calcite prisms for the polarizer and analyzer and two Faraday rotators to vary the plane of polarization. Images collected as the plane of polarization is varied are processed using a single-frequency Fourier filtering algorithm to calculate the magnitude of retardation on a pixel-by-pixel basis. This approach has the advantage of maintaining high extinction optics throughout the optical train and it exploits the full swing of the birefringent signal as the polarization angle is modulated. In addition, the single-frequency Fourier filter is computationally fast, a feature that is important in studies of living cells.

MATERIALS AND METHODS

Cell culture

Culture media including Roswell Park Memorial Institute (RPMI), Dulbecco/Vogt modified Eagle's (DMEM), Hank's Balanced Salt Solution (HBSS), tissue culture grade HEPES, Fetal Bovine Serum (FBS), 10X trypsin stock, pyruvate, glutamine, penicillin, and streptomycin were obtained from Gibco BRL (Grand Island, NY). REF-52 cells, provided as a gift by Dr. James Feramisco, were grown in RPMI supplemented with 24 mM $NaHCO_3$, 100 units/ml penicillin, 100 mg/ml streptomycin and 10% FBS.

The cloned allospecific cytotoxic T lymphocyte cell (CTL) line, BM3.3, was a gift from Dr. Anne-Marie Schmidt-Verhulst (Centre de Immunologie, CNRS-INSERM, Marseille, France). BM3.3 CTLs were stimulated weekly with irradiated spleen cells from C57BL/6 mice and maintained in standard RPMI supplemented with 1 mM pyruvate, 1 mM glutamine, 10^{-4} M β-mercaptoethanol and 10% IL-2 supernatant prepared from EL4-C16 cells as described by Farrar et al. (1980). The EL4.BU cell line, which serves as an antigenic target for BM3.3, was maintained in RPMI containing 10% FBS.

The cloned CTL line CTL3, was used for expression of a GFP-tubulin plasmid. This is an allospecific CTL line that shows differential specificity for killing ($H\text{-}2^k \gg H\text{-}2^d$) versus proliferation ($H\text{-}2^d \gg H\text{-}2^k$; Russell and Dobos, 1983). CTL3 cells were stimulated weekly with irradiated spleen cells from $H\text{-}2^d$ (BALB/c) mice and were maintained in MEM supplemented with 5% heat inactivated FBS, 12% T-Stim (Collaborative Biomedical Products, Bedford, MA), 100 IU penicillin and 100 μg/ml streptomycin.

Microscopy

For microscopy REF-52 cells were grown on 25-mm round glass coverslips in growth media. For short observations, coverslips were attached with silicon vacuum grease to the bottom of a 35-mm-diameter round petri dish containing a hole of about 15-mm diameter. A few drops of HBSS + HEPES buffer was added and a second, clean coverslip was placed on top and sealed with vacuum grease to form a window approximately 1-mm thick.

Transfection of CTL3 cells with GFP-tubulin

A GFP-tubulin plasmid was obtained from Clontech (pEGFP-Tub; Palo Alto, CA). Plasmid DNA was amplified and purified using a Qiagen Plasmid Maxi Kit (Qiagen, Valencia, CA). In preparation for electroporation, CTL3 cells were plated out in 24-well plates at 70% confluence the day before use. Immediately prior to electroporation, $2\text{–}2.5 \times 10^6$ cells were pelleted and resuspended in phosphate buffered saline (PBS) (8.0 g/L NaCl, 0.2 g/L KCl, 1.44 g/L Na_2HPO_4, and 0.24 g/L KH_2PO_4, PH 7.2), then pelleted and resuspended again in 100 μL fresh PBS along with 20 μg circular plasmid DNA and left on ice for 10 min. The cell suspension was then placed in a 0.4-cm cuvette-electrode and electroporated at 200 Volts and 250 μF using a Gene Pulser II system (Bio-Rad, Hercules, CA). After electroporation, cells were diluted into 4 ml culture media and incubated at 37°C for 24 h. Subsequently, cells were maintained in 0.3 mg/ml Genetecin to select for stable transfectants.

Instrumentation

Differential Interference Contrast (DIC) pictures were taken on a Nikon Diaphot-200 microscope using a Nikon oil-immersion 1.4 NA 60× DIC objective lens and an oil-immersion 1.4 NA DIC condenser lens (Nikon, Inc., Melville, NY). Images were digitized with a 12-bit, cooled CCD camera (C4742-95, Hamamatsu Corp., Bridgewater, NJ) using a National Instruments (Austin, TX) PCI-1424 frame grabber. Phase contrast pictures were taken with an oil-immersion 1.3 NA 100× Zeiss objective lens and matching 1.4 NA oil-immersion condenser on a Zeiss "Research 18" microscope (Carl Zeiss, Inc., Thornwood, NY). Phase images were recorded with a Dage-MTI CCD72 camera (Michigan City, IN) and digitized using Scion AG5 image processing hardware (Scion Corp., Frederick,

MD). GFP-tubulin transfected cells were viewed with a Nikon Diaphot-TMD microscope using a 1.4 NA 100× oil-immersion objective and a Chroma technologies (Brattleboro, VT) GFP filter set. Images were recorded with a Dage-MTI SIT-66 intensified camera.

The modulated polarization microscope (MPM) uses a Nikon inverted Diaphot-TMD microscope equipped with a 1.4 NA DIC oil immersion condenser, and either a 1.4 NA 60× DIC oil-immersion objective, or a 1.4 NA 100× DIC oil-immersion objective lens (see Fig. 1). The polarizer for the system is a cemented Glan–Thompson-type calcite prism, whereas the analyzer is an air-gap Glan–Taylor prism. The polarization angle was modulated by two custom-made Faraday rotators (Azzam, 1978), one positioned above the condenser and the other below the objective. These Faraday rotators each consist of a specially compounded glass rod and a water-jacketed solenoid. The glass rods were made by Kigre Inc. (Hilton Head, SC) using Terbium-doped M-32 glass (2-cm diameter by 4-cm with a Verdet constant of 0.5 min/Oersted-cm at 546 nm). The rods were subsequently polished and coated by Karl Lambrecht Corporation (Chicago, IL).

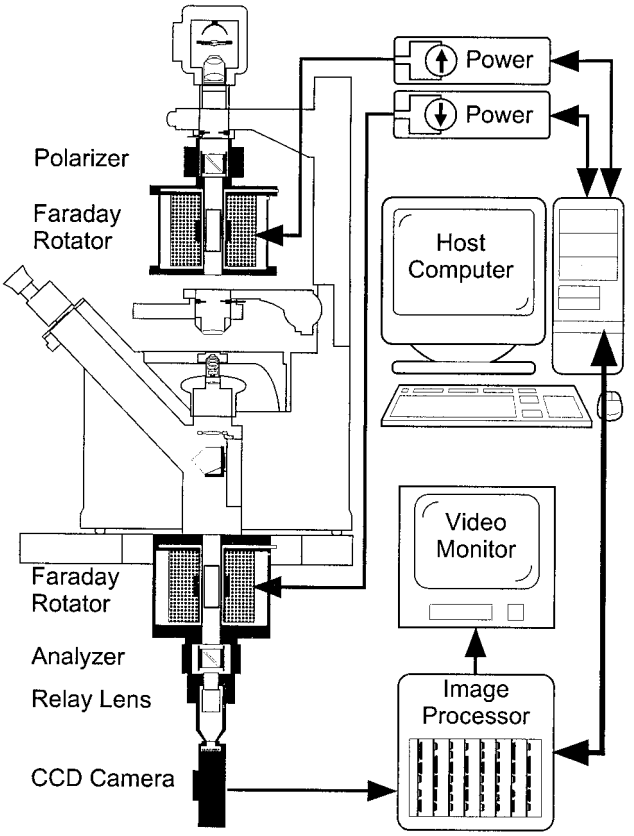

FIGURE 1 A schematic illustration of the microscope. A Nikon Diaphot inverted microscope was modified to support two Glan-type prism polarizers and two Faraday effect, magneto-optic polarization rotators. Bipolar power sources supply current to the solenoid magnets such that the amount of polarization rotation generated in the first solenoid is cancelled by the second. The polarizer and analyzer remain in their fixed, crossed orientation, and an analog CCD camera captures the image as the polarization direction is varied from −45 to +45°. Video images are captured and digitally processed by a single-frequency Fourier filter implemented on a Datacube MaxVideo image processing system. A PC host computer controls timing of both the image-processing algorithm and the polarization rotation. Resulting MPM images may be displayed on a video monitor or sent to the host computer for storage as a movie file.

The solenoid is formed on an aluminum spool whose hollow aperture houses the glass rod. Each spool winding was designed with a cutout to give straight magnetic field lines running parallel to the long axis of the glass rod (see Montgomery, 1980) and provides a central field strength of 68 Oersteds per Ampere. Because the amount of both rotation and absorption by the M-32 glass increases as the wavelength decreases, the 436-nm mercury line was chosen as a compromise between maximum rotation and minimum absorption by the M-32 glass. At this wavelength, the Faraday rotators provide an angular rotation of 3.3 degrees per Ampere and have a transmission coefficient of 58%.

Due to the high operating current, it was necessary to cool the solenoid windings with running water, which was achieved by placing the spool inside a sealed aluminum housing. Even with cooling, the central glass rod became warmer over time, which reduced the rotation at a given current. To compensate for this effect, the winding resistance was measured once every minute to estimate the temperature increase within the solenoid. Because rotation drop was found to be linear with resistance, this resistance measurement could be used to calculate a slight current increase that would bring the rotation back to its previous value. This temperature compensation method kept the rotation constant until the temperature within the solenoids stabilized, typically after twenty minutes.

Current to the solenoids was provided by two BOS/S 20-20 computer-controlled DC power supplies (Electronic Measurements Inc., Tinton Falls, NJ) each capable of delivering ±20 Amperes at 400 Watts. The power supplies were connected to the two Faraday rotators with opposite polarity such that any given rotation angle produced by the first Faraday rotator was canceled by the second. This arrangement allowed the specimen to be presented with polarized light of varying angle and yet viewed at full extinction as if the polarization angle was fixed.

Optical measurements

The Modulation Transfer Function (MTF), anisotropy, resolution, and extinction values for the extended optical train were determined using a Richardson Test Slide (Model 80101, Bio-Microtech Inc., Bolton, Ontario, Canada). This test slide contains sets of evenly spaced bars having inter-bar spacings of 4 μm, 2 μm, 1 μm, 500 nm, 250 nm, and 200 nm. All measurements were made at 436 nm using a 1.4 NA 100× DIC oil-immersion objective lens and a 1.4 NA DIC condenser lens set to ⅔ aperture (NA = 0.93). Images of the bar patterns on the test slide were captured using a 12-bit, cooled CCD camera (C4742-95, Hamamatsu Corp.). Because the theoretical maximum resolution is 190 nm for 436-nm light, enough magnification was used to allow the camera to sample images at 40–60 nm/pixel. These sampling sizes were therefore well below the Nyquist criteria of 95 nm/pixel needed to capture the maximum resolution without sampling error.

The MTF and anisotropy of the system were calculated from the bar pattern images using a custom plugin for ImageJ (http://rsb.info.nih.gov/ij/) written to implement the method of Sitter et al. (1995) for estimating MTF. For each set of bar patterns, the intensity was measured along a line extending across at least five bars, and the Fourier transform of each resulting intensity plot was used to estimate the MTF for that bar frequency. To assess measurement error, the line profile was taken at four different positions across each pattern in the image, the slide was refocused, and the entire measurement was repeated four times, giving a total of sixteen MTF measurements per bar spacing. To eliminate any anisotropy due to differences between the horizontal and vertical bar patterns on the slide, the horizontal bars were rotated to the vertical position for vertical measurements.

The numerical aperture of the extended optical system was determined from an image of the entire collection of parallel bars. The Fourier transform of this image reveals the exit pupil or cutoff frequency as a circular aperture whose diameter varies according to the number of harmonics captured by the optics. The resolution of the system (d) was estimated by measuring the radius (r) from the center (zero frequency) of

the Fourier spectrum to the edge of this circular aperture. The resolution is then determined as $d = 1/r$ and the numerical aperture is calculated from the equation $NA = 0.61\lambda/d$.

Extinction of the extended optical system was measured using a Pacific Instruments Photometer (Model 126, Concord, CA) to measure the intensity with polarizers parallel, I_P, and the intensity with crossed polarizers, I_C. The extinction factor, defined as $EF = I_C/I_P$, was measured for both crystal and standard film (HN22) polarizers. A neutral density filter (Melles Griot, Irvine, CA) with a known optical density of 2.983 was added in the optical path to place I_p in approximately the same range as I_C and circumvent any nonlinearity in the photometer output. Because the sensitivity of the photomultiplier varied slightly with polarization angle, the photomultiplier tube was always rotated in concert with the analyzer. All intensity measurements were repeated five times to estimate measurement error.

Filtering

The polarization angle is modulated by varying the current to the Faraday rotators (frequency is user adjustable, from 0.25 to 2 Hz.). Image acquisition is synchronized to rotation of polarization angle such that successive frames are captured as the polarization angle is ramped linearly between −45 and +45°. Video images are acquired by a Dage-MTI CCD72 camera (Michigan City, IN), and digitized and processed at 30 frames per second using a single-frequency Fourier filter implemented on a DataCube (Danvers, MA) Maxvideo image-processing system. The polarization angle is typically modulated at 1 Hz to give one fully processed MPM image per second.

The single-frequency Fourier filtering algorithm is described as follows. The intensity $I(t)$ of a birefringent object (as seen by the camera) will vary sinusoidally with the changes in polarization angle, $\theta(t)$. The amplitude of this sinusoidal variation depends on the specimen retardance R, the angle of the specimen's fast axis ϕ, and the maximum intensity obtained with parallel polarizers, I_P (Allen et al., 1963, 1966). Because polarizers do not have perfect extinction, a small term representing the background light with crossed polarizers, I_C, is added to the intensity equation to give

$$I(t) = I_P \sin^2(R/2)\sin^2(2\theta(t) - 2\phi) + I_C. \quad (1)$$

As the polarization angle, $\theta(t)$, is rotated through 90° over a short period, T, the intensity of a birefringent specimen will oscillate with an amplitude of A, that depends on its retardance. The phase offset (whether it varies as a sine or cosine wave) depends on the orientation of the specimen (i.e., ϕ). The best way to find the amplitude of any periodic signal is to find its Fourier series coefficients, a_0, a_1, a_2, a_3, . . . and b_1, b_2, b_3, ... *These coefficients describe the constant offset of the signal*, a_0, the cosine and sine amplitudes of the fundamental frequency, a_1 and b_1, respectively, the amplitudes of the first harmonic, a_2 and b_2, and so forth. The term a_0 is simply the average of the signal. The remaining coefficients are obtained by multiplying the intensity output by a cosine or sine function and integrating.

$$a_0 = (1/T)\int_0^T I(t)\,dt \quad (2)$$

$$a_n = (2/T)\int_0^T I(t)\cos(n2\pi t/T)\,dt \quad (3)$$

$$b_n = (2/T)\int_0^T I(t)\sin(n2\pi t/T)\,dt. \quad (4)$$

Because the polarization angle changes linearly, there are no higher-order harmonics, making the coefficients a_2, a_3, a_4, . . . and b_2, b_3, b_4, . . . all zero. The average, a_0, arises from constant portions of the signal, which constitute an unwanted background signal. The signal amplitude thus depends solely on the fundamental frequency components a_1 and b_1 which can be determined on pixel-by-pixel basis as

$$a_1 = (2/T)\sum_{t=1}^{T} I(t)\cos(2\pi t/T) \quad (5)$$

$$b_1 = (2/T)\sum_{t=1}^{T} I(t)\sin(2\pi t/T). \quad (6)$$

The amplitude of the signal swing is then the geometric mean of a_1 and b_1, and is related to birefringence by the relationship

$$A = (a_1^2 + b_1^2)^{1/2} = (I_P/2)\sin^2(R/2), \quad (7)$$

whereas the orientation of the object's fast axis can be obtained from the arctangent

$$\phi = \tan^{-1}(b_1/a_1). \quad (8)$$

It should be noted that the value of $\sin^2(2\theta - 2\phi)$ is the same whether specimen orientation is $\phi = 0°$ or $\phi = 90°$. Thus, MPM cannot unambiguously distinguish between the slow and fast axes of a specimen without a reference point in the form of a compensator.

The amplitude can be scaled to a reasonable gray-scale range and displayed as a birefringence image. This normally provides a good image of cell structure. However, a small amount of background signal swing usually contaminates the image. Most of this is due to polarization aberrations arising from strain birefringence and curvature of the lenses (Hansen, 1988). In principle, this background can be removed by moving to a blank microscope field and recording separate images for each polarization position $B(t)$. Each of these images would then be subtracted from the corresponding specimen image before performing the integration:

$$a_1' = (2/T)\sum_{t=1}^{T}[I(t) - B(t)]\cos(2\pi t/T) \quad (9)$$

$$b_1' = (2/T)\sum_{t=1}^{T}[I(t) - B(t)]\sin(2\pi t/T) \quad (10)$$

However, these background images can be factored out of the summation, such that only two processed "background" Fourier coefficients, a_{back} and b_{back}, need be stored. These background coefficients can then be subtracted before taking the geometric mean as follows:

$$a_1' = a_1 - (2/T)\sum_{t=1}^{T} B(t)\cos(2\pi t/T) = a_1 - a_{back}, \quad (11)$$

$$b_1' = b_1 - (2/T)\sum_{t=1}^{T} B(t)\sin(2\pi t/T) = b_1 - b_{back}, \quad (12)$$

$$A' = (a_1'^2 + b_1'^2)^{1/2}. \quad (13)$$

This background subtraction method proves to be adequate for removing most or all of the background birefringence.

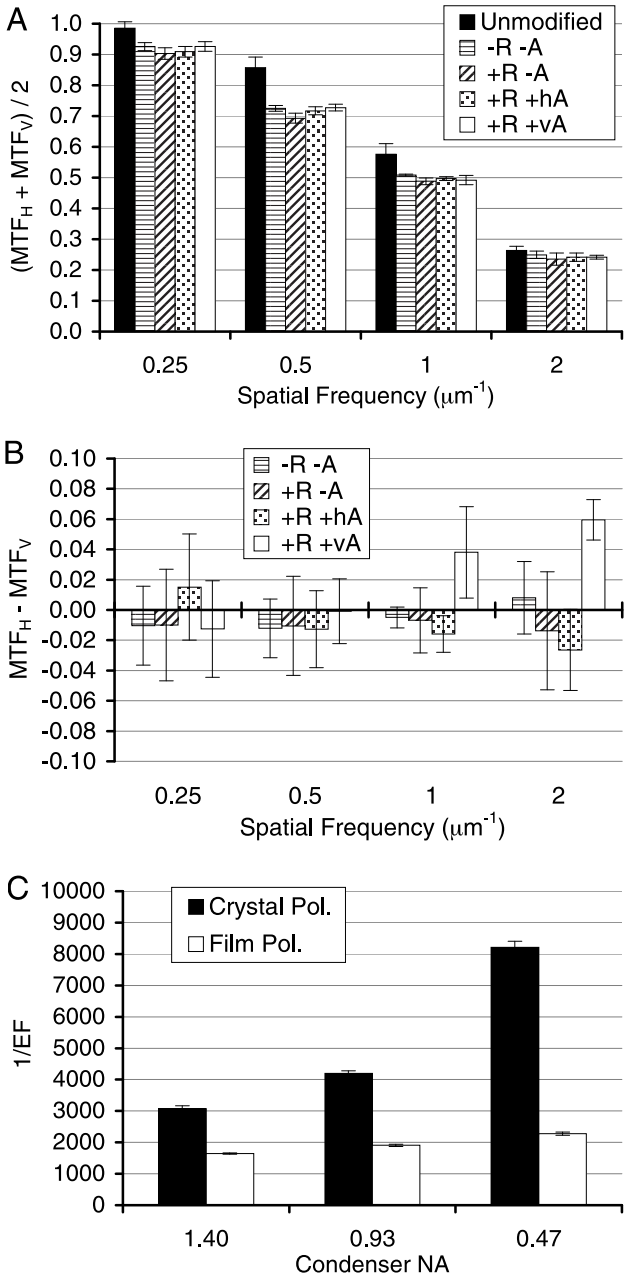

FIGURE 2 Optical performance of the modified microscope. The modulation transfer function of the extended optical system was measured using a series of finely spaced bar patterns with inter-bar spacings of 4 μm, 2 μm, 1 μm, and 500 nm. Due to the possibility of astigmatism, the MTF was measured for the same set of bars rotated to either the horizontal or vertical direction. (*A*) To determine how the modifications of the optics affect image quality, the mean MTF, $(MTF_H + MTF_V)/2$, was used to compare the performance of the microscope under five different optical arrangements: standard tube length (*Unmodified, black bar*), extended optical path with no added optical elements ($-R\ -A$, *horizontally striped bar*), extended path with both Faraday rotator rods but no analyzer ($+R\ -A$, *diagonally striped bar*), extended path with both Faraday rotator rods and the horizontal analyzer ($+R\ +hA$, *stippled bar*), extended path with both Faraday rotator rods and the vertical analyzer ($+R\ +vA$, *white bar*). (*B*) As a test for astigmatism, the MTF data for the extended optical system obtained above was plotted as the difference between the horizontal MTF and the vertical MTF. Here, the abscissa has been expanded to reveal the small differences in MTF for the horizontal and vertical directions. (*C*) Extinction values for the complete microscope optical train were measured using either crystal polarizers (*black bar*, normal configuration) or film polarizers (*white bar*, Polaroid HN22). Because the extinction factor (here plotted as 1/EF for clarity) varied with condenser aperture, the measurements were made at three different condenser settings: full aperture (NA = 1.4), ⅔ aperture (NA = 0.93), and ⅓ aperture (NA = 0.47). All measurements were performed using a 1.4 NA 100× oil-immersion objective and a 1.4 NA oil-immersion condenser lens under conditions similar to the typical MPM measurement.

Typically, 32 frames are processed at video rates to give one MPM image per second (1 Hz). This proved to be adequate for observing many types of cell movements. At present, the upper speed limit is 2 Hz because of the inability to write more than 2 frames per second to the disk. Because the analog camera has a fixed frame rate, faster imaging speeds means reducing the number of frames processed and increasing image noise. Stationary or slow-moving objects can benefit from slower imaging rate because processing more frames reduces the noise.

RESULTS

Optical characterization

The prototype MPM system was designed around a modified Nikon Diaphot microscope (see Fig. 1). These modifications included lengthening of the optical path to accommodate the Faraday rotators and calcite polarizers. The Faraday rotators were initially developed using 2-cm-diameter rods custom made using high Verdet constant glass. Rods of this size were less than ideal but were chosen as a compromise due to their expense and the increase in magnet power needed to accommodate larger-diameter rods. As expected, the extension of the optical path and the limiting aperture of the lower Faraday rotator decreased the total numerical aperture of the system. Using an oil-immersion 1.4 NA 100× DIC objective, the NA of the extended path was found to be 0.80 ± 0.02, corresponding to a resolution limit of 332 ± 8 nm. This was a decrease from the 1.35 ± 0.05 NA measured for the unmodified microscope.

Any decrease in image quality due to the increased tube length, limiting aperture, and added optical elements should be reflected as a change in the modulation transfer function of the microscope. To assess these effects, the MTF was measured using a test slide containing a series of horizontal and vertical bar patterns with spacings of 4 μm, 2 μm, 1 μm, and 500 nm for both the normal tube length, and for the extended MPM form of the microscope. Although bar spacings of 250 and 200 nm were included on the test slide, they were below the resolution limit of 332 and were not included in MTF measurements. Figure 2 *A* shows the average MTF measured for the unmodified microscope and for the extended optical path, with or without the Faraday rotator rods and the analyzer. Comparison of the unmodified microscope (*Unmodified*) to that of the extended optical path with no added optics ($-R\ -A$) shows a slight reduction

in MTF. When the Faraday rotator rods are included in the extended optical path ($+R\ -A$) there is an additional small reduction in MTF. In contrast, addition of a crystal analyzer in either horizontal ($+R\ +hA$) or vertical ($+R\ +vA$) orientation increased the MTF slightly, negating the effects of the glass rods. Overall, the results show that the extended tube length and reduced aperture of the modified microscope gave a small decrease in the MTF at all spatial frequencies when compared to that of the unmodified microscope.

The rotator rods and crystal polarizers act essentially as large refracting optical flats. Any asymmetry, tilt, or surface warping of either the rotator rods or the polarizers could potentially produce astigmatism in the image plane. To determine whether these elements introduced any astigmatism, the difference between the MTF measured for horizontal and vertical bars was calculated and is shown in Fig. 2 *B*. Although the glass rotator rods did not add any additional astigmatism to the system (bar $+R\ -A$), the crystal analyzer introduced a slight astigmatism in the MTF that shifted from horizontal to vertical as the analyzer was rotated (bars $+R\ +hA$ and $+R\ +vA$). Because Glan-type calcite polarizers have a different acceptance angles in each direction (Bennett, 1995), some astigmatism at higher spatial frequencies was expected. However, the 500, 250, and 200-nm bar patterns were found to be substantially brighter when viewed between crossed polarizers. Any polarization produced by the bar patterns could account for some of the increased astigmatism seen at high spatial frequencies when only one polarizer was placed in the light path.

Although the crystal polarizers introduce a slight astigmatism, they also provide better extinction than film polarizers. Figure 2 *C* compares the extinction factor measured for the entire optical system using either film or crystal polarizers. Because the difference in extinction value between crystal and film polarizers varies with condenser aperture, extinction values were measured at three condenser settings. The results show that, for all aperture settings, the crystal polarizers give better extinction than film polarizers. However, the difference between crystal and film polarizers is much greater at reduced apertures. This difference is readily explained by examining the image in the back focal plane as the aperture is reduced. In polarized light, the image in the back focal plane is a dark cross with four bright lobes that arise from depolarization at the curved surfaces of the lenses (Inoué and Hyde, 1957). High-extinction crystal polarizers produce a darker cross than film polarizers but they do not affect the presence of the bright lobes. Reducing the condenser aperture suppresses the bright lobes so that the extinction is more closely related to the overall darkness of the cross. Because of this effect, MPM experiments were typically performed with the condenser in the ⅔ to ⅓ range, for a $\log_{10}EF$ of between -3.623 ± 0.009 and -3.915 ± 0.010.

Performance of MPM

The performance of MPM with biological samples was initially tested using the Swiss 3T3 and REF 52 fibroblast cell lines due to their conspicuous stress fibers. Figure 3 illustrates how the modulated polarization microscope enhances the contrast of these stress fibers. For comparison, the first picture (Fig. 3 *A*) shows an image of a Swiss 3T3 cell obtained without modulating the plane of polarization. Subsequently, a series of images was obtained from the same cell as the polarization angle was stepped from −45 to +45° (Fig. 3 *B*). Although many of the stress fibers are too faint to detect, the brightness of some of the larger ones (*arrows*) do change visibly as the polarization angle is rotated. Figure 3 *C* shows an image of the same cell obtained by continuously varying the polarization angle and processing the images using the single-frequency Fourier filtering algorithm. Note that some filaments that are obvious in Fig. 3 *C* are not detectable in Fig. 3 *A*.

To quantify the improvement in contrast afforded by MPM, line plots of image pixel intensities were analyzed for contrast before and after MPM modulation and filtering. The polarized light image used for comparison to MPM was the one showing best overall contrast out of a set of images taken at sixteen different polarization angles (Fig. 3 *A*). Figure 4 *A* shows a plot of pixel values along the line shown in Fig. 3 *A*. From this data, a plot of the background was also obtained using a rolling-ball averaging algorithm. Pixel values and the calculated background of the same line of pixels were also plotted for the processed MPM image (Fig. 4 *B*). These calculated backgrounds were then used to determine image contrast values, here defined as the absolute value of the difference between pixel intensity and the background intensity, divided by the background intensity. Contrast values are plotted in Fig. 4 *C*. The results show that MPM gives an improvement in contrast typically in the range of 40- to 100-fold over conventional polarized light microscopy.

To compare the cellular detail detected by MPM to that of other types of microscopy, REF-52 fibroblasts were imaged by MPM, phase contrast, DIC, and fluorescence microscopy (Fig. 5). Figure 5, *A* and *B*, show example MPM images of living fibroblasts. In most cells, one also can see numerous elongate vesicular structures, possibly mitochondria, closely associated with these stress fibers. The enhancement of vesicle contrast was an unexpected feature of MPM and is probably due to edge birefringence of vesicle membranes. Continuous recording showed that one of these vesicles moved considerable distances along the stress fiber. The level of structural detail that one sees depends to some extent on the density of stress fibers. In Fig. 5 *B*, the high density of stress fibers tends to obscure the vesicles (*arrowheads*) that, although present, are difficult to discern.

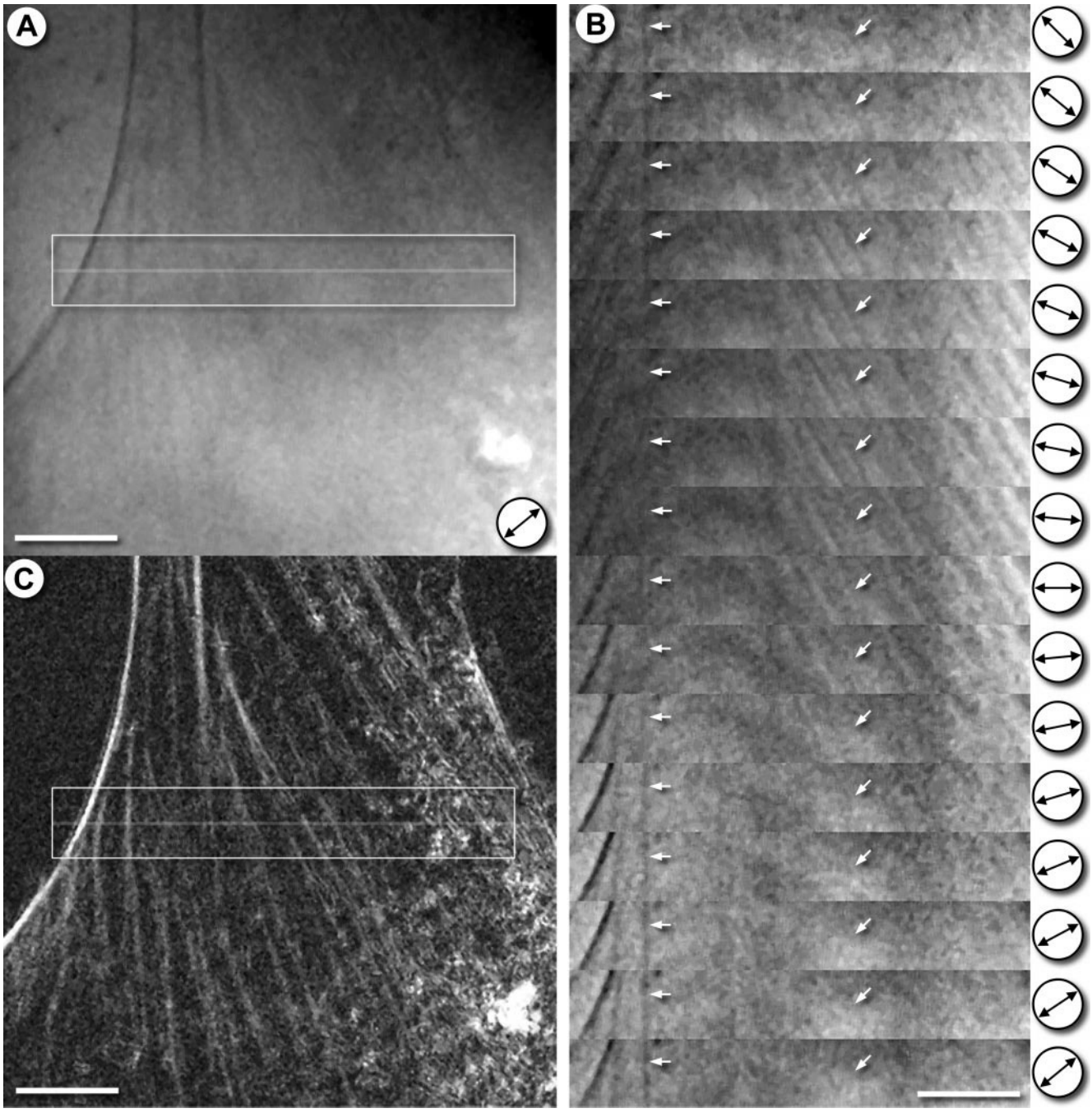

FIGURE 3 Demonstration of MPM modulation and processing. Swiss 3T3 fibroblasts were observed by polarized light microscopy or by MPM. (*A*) Polarized light image of the cell as seen when no power is applied to the solenoids. This is equivalent to viewing the cell through fixed crossed polarizers at full extinction. (*B*) A series of images from the same cell as the polarization angle is varied. For the sake of space, a fixed region of interest (box in *A*) was chosen for display. The polarization angle for each image in the series is displayed to the right. Because the second Faraday rotator is set to cancel the rotation produced by the first, the image at each polarization angle is effectively viewed through crossed polarizers. Specific examples of fibers that change their intensity as the polarization angle is varied are denoted by arrows. (*C*) The fully processed MPM image is obtained by processing the series of images shown in *B* using the Fourier filtering algorithm. Scan lines indicated in the center of the boxes in *A* and *C* were further analyzed for the contrast comparisons shown in Fig. 4. All images were obtained using an oil-immersion 60× 1.4 NA objective lens. Scale bars are 10 μm.

To determine whether filamentous structures seen in Fig. 5, *A* and *B*, represent true stress fibers or might be some artifact of MPM imaging, fibroblasts were fixed and stained with rhodamine-phalloidin and then imaged both by fluorescence microscopy (Fig. 5 *C*) and by MPM (Fig. 5 *D*). It should be noted that, when viewed by MPM, fixed cells

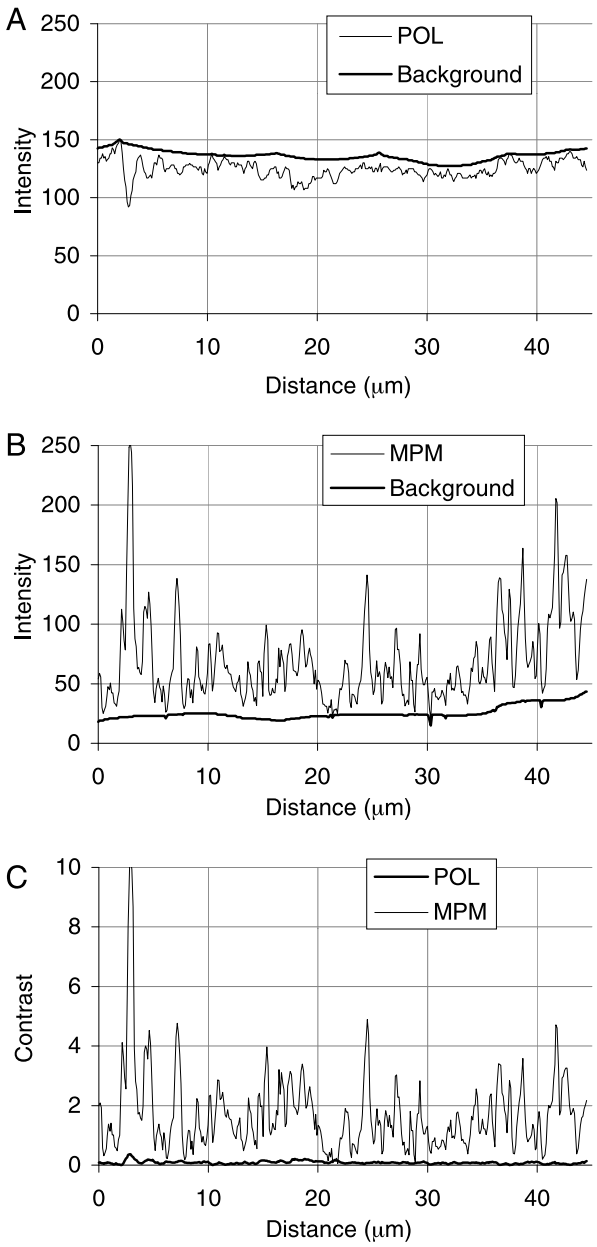

FIGURE 4 Contrast analysis of polarized light and MPM images. Scan lines of pixel intensities from the images shown in Fig. 3, *A* and *C*, were analyzed for contrast. Pixel value plots of both the original polarization image (*A, POL*) and the MPM processed image (*B, MPM*) are shown, as are the background intensities calculated using two-dimensional rolling-ball averaging. For the POL image, because the visible stress fibers were darker than the background, an inverted rolling-ball average was used as the background. The calculated intensities of the background and the pixel values from the scanlines were used to calculate the contrast value, shown in *C*, for both POL and MPM images.

generally give less cytoskeletal detail than living cells. Even so, one can readily see that the fibers stained by rhodamine-phalloidin are the same fibers seen by MPM.

Images of living REF-52 cells obtained by MPM were also compared to those obtained by DIC and phase microscopy, two other optical contrast techniques commonly used to study the cytoskeleton. Because the MPM instrument was not equipped with phase contrast or DIC optics, different preparations were imaged using separate MPM, DIC, and phase contrast microscopes. Although this is not the ideal way to compare the capabilities of each instrument, the stress fibers in these fibroblasts are quite prominent and similar from one cell to the next. Thus, the observed differences are primarily a function of the various microscopy methods rather than differences between individual cells.

Typical images obtained using DIC and phase contrast microscopes are shown in Fig. 5, *E* and *F*, respectively. In both cases, structures resembling stress fibers can be seen in the thin lamellae of the cells. However, for both DIC and phase, those stress fibers that are visible become obscured as one moves to thicker portions of the cell. In the case of MPM, stress fibers are clearly seen throughout the cell. Even within lamellae, where DIC and phase contrast optics work best, stress fibers are still much less numerous and prominent than those detected by MPM.

Imaging microtubules by MPM

The main motivation for developing MPM microscopy was to study cytoskeletal polarization that occurs during CTL–target cell interactions. One of the striking features of this event is the repositioning of the microtubule organizing center (MTOC) in the CTL when it is activated by an antigenic target cell (Geiger et al., 1982; Kupfer and Dennert, 1984). In principle, MTOC dynamics could be studied by transfecting CTLs with GFP-tubulin. However, when CTL3 cells were transfected with a plasmid containing GFP-tubulin, the results were disappointing. Figure 6 shows samples of fluorescence images of CTLs expressing GFP-tubulin. Most of the cells exhibit a relatively uniform green fluorescence (Fig. 6 *A*). Occasionally microtubules can be seen against this green background (Fig. 6 *B*) but in these cases they are most evident near the MTOC rather than at the periphery of the CTL. Fluorescence images such as these do not reveal much detail regarding interactions of microtubules at the target contact site where MTOC polarization is thought to be initiated.

MPM gives much clearer and sharper images of microtubules than the fluorescence images of cells expressing GFP-tubulin. For example, Fig. 7 *A* shows an MPM image of a BM3.3 CTL plated in the absence of target cell. Here, one can see numerous microtubules originating at a point near the nucleus and extending out to the periphery of the cell. In the video file from which this image was taken, these microtubules exhibited wave-like movements that repeatedly brought portions of microtubules in and out of focus. The origin of microtubules at the MTOC was also obscured by birefringent vesicles that appear to lie on top of the MTOC.

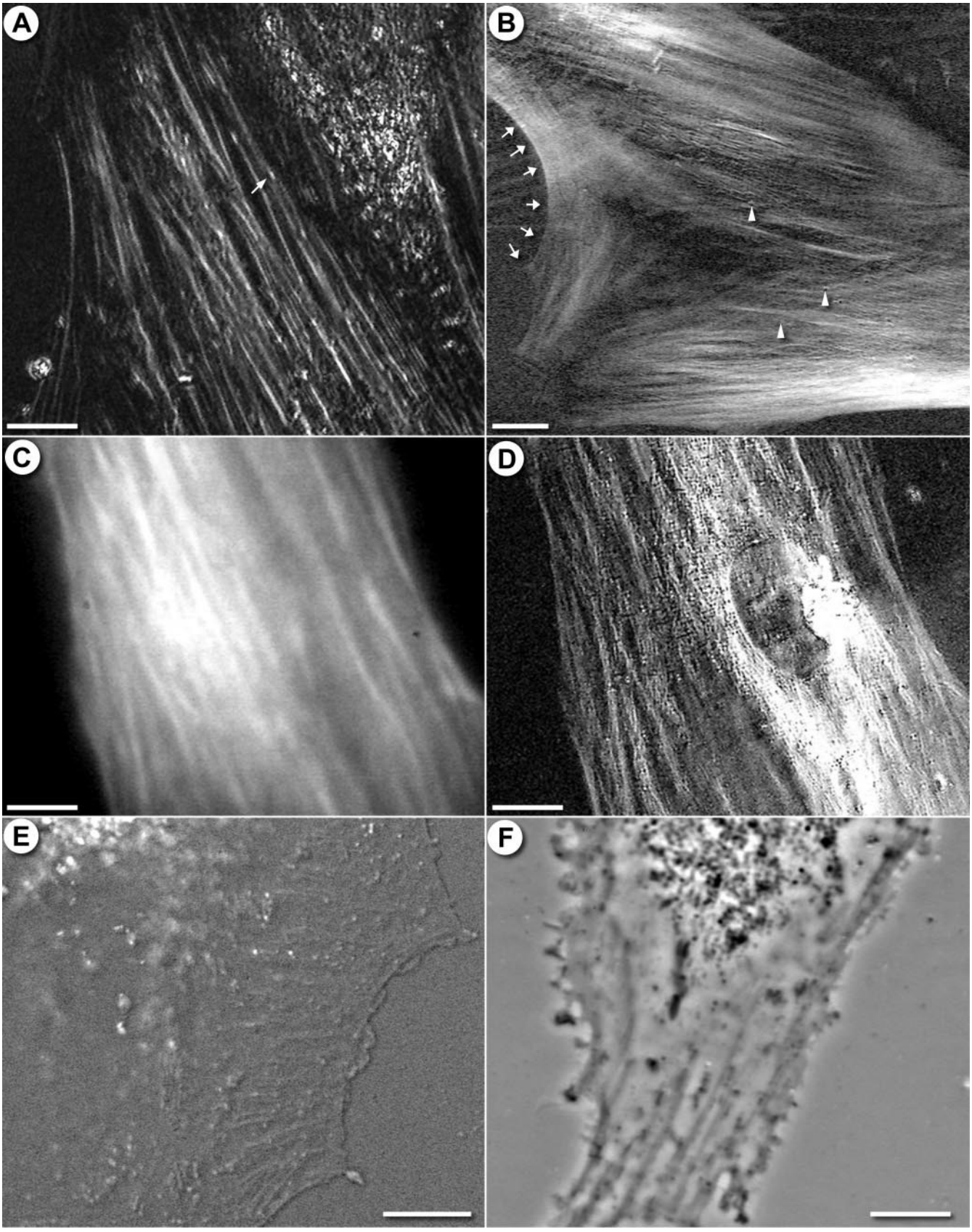
A
B
C
D
E
F

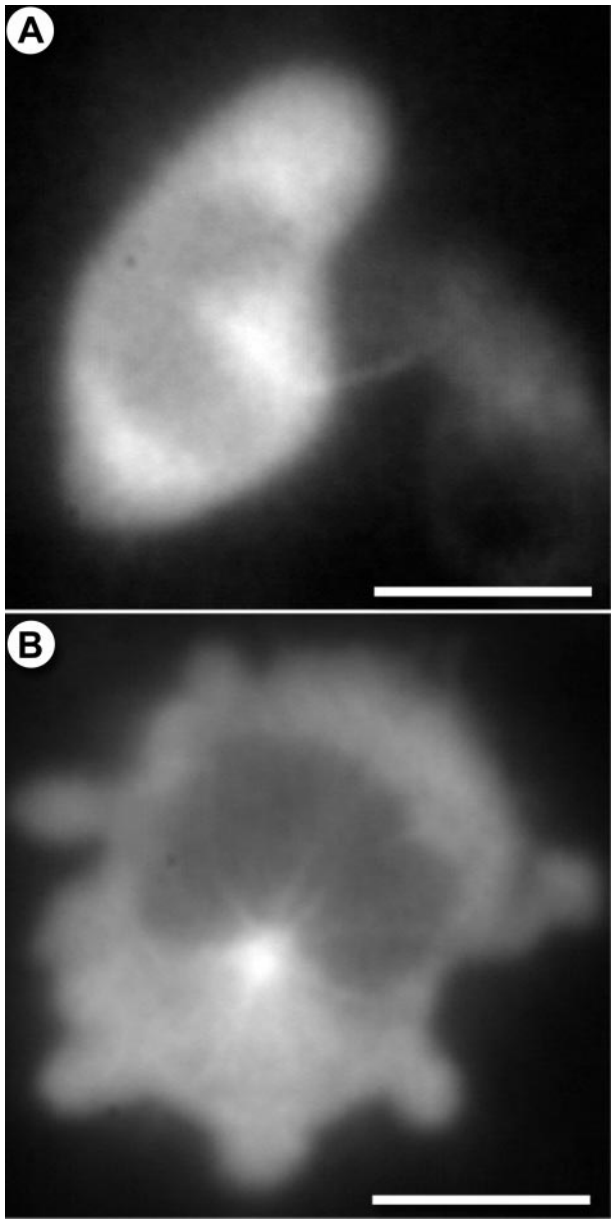

FIGURE 6 Fluorescence images of GFP-tubulin transfected cytotoxic T lymphocytes. CTL3 CTLs transfected with GFP-tubulin were imaged by fluorescence microscopy. An image representative of most of the transfected cells is shown in (*A*). Here individual microtubules were completely obscured by the diffuse cytoplasmic fluorescence. (*B*) In exceptional cases, some microtubules near the MTOC could be distinguished. *A–B* were obtained using an oil-immersion 100× 1.4 NA objective lens. Scale bars are 10 μm.

In Fig. 7 *B*, BM3.3 CTLs were plated together with antigenic target cells (EL4.BU). In this case, the CTL (*C*) has bound to a target cell (*T*) and the MTOC has already repositioned next to the target contact site. Here, one can see numerous microtubules pointing away from the MTOC. This MTOC polarization is typical of what is seen when CTL–target cell pairs are immunostained for tubulin. In a study to be detailed elsewhere, the process of MTOC polarization was monitored in real time by MPM. These data show the entire process of CTL-mediated killing including MTOC movements and target cell lysis.

To determine whether MPM reveals more cellular detail than can be detected by other types of transmitted light microscopy, CTLs were also imaged by DIC and phase contrast microscopy. Example images are shown in Fig. 7, *C* and *D*, respectively. In the case of DIC, the thickness of the CTL and the presence of large dense vesicles makes it difficult to see much cytoskeletal detail. The most obvious structures in the cell were numerous large and small vesicles. On occasion, we could see linear structures resembling microtubules, but, on closer examination, these were actually chains of vesicles that may have been attached to microtubules. In phase contrast microscopy, the images were generally less sharp and nothing resembling microtubules was evident.

One of the characteristic features of MPM is its ability to enhance the contrast of vesicles and cytoskeletal elements. CTLs contain numerous large vesicles which, when imaged by MPM, exhibit bi-directional movement along microtubules. An example of this can be seen in the series of images shown in Fig. 8. Although the images are of lower resolution than those shown in Fig. 7, one can still see numerous microtubules radiating out from a central point. Once again, due to the optical sectioning property of MPM, only a subset of the microtubules is visible in any given plane of focus. In the short segment shown Fig. 8, *A–D*, one can follow the movements of two different vesicles that are associated with two different microtubules. As the sequences progresses one vesicle (*arrow*) moves inward toward the MTOC while the other (*arrowhead*) moves outward toward the periphery of the cell. Over the entire course of the movie, most of the vesicles that are visible in Fig. 8 moved repeatedly back and forth. In every case, they closely followed one of the microtubule tracks.

FIGURE 5 The fibroblast cytoskeleton as seem by MPM, fluorescence, DIC, and phase contrast. (*A*) MPM image of a live REF-52 fibroblast shows both stress fibers and vesicular structures (possibly mitochondria) that travel along these fibers. Continuous recording of this cell showed that most of these vesicles are stationary but the vesicle designated by the arrow could be seen moving along the fiber. (*B*) MPM image of a living Swiss 3T3 fibroblast. The 3T3 cell shows much finer, more evenly distributed stress fibers compared to the REF 52 cells. Note that fiber orientation does not affect their visibility by MPM. Although most fibers run diagonally across the image, the curved fibers running vertically (*arrows*) are equally bright. Vesicles (*arrowheads*) are also visible in the midst of the stress fibers. To determine the relationship between the fibers seen in MPM and stress fibers, a fixed Swiss 3T3 fibroblast was stained with rhodamine phalloidin. The actin filament-based stress fibers seen in the fluorescence image (*C*) are identical to the fibers seen in the MPM image (*D*). For comparison, typical DIC (*E*) or phase contrast (*F*) images of REF-52 fibroblasts are also shown. *A–E* were obtained using an oil-immersion 1.4 NA 60× objective lens. Image *F* was obtained using an oil-immersion 1.3 NA 100× objective lens. Scale bars are 10 μm.

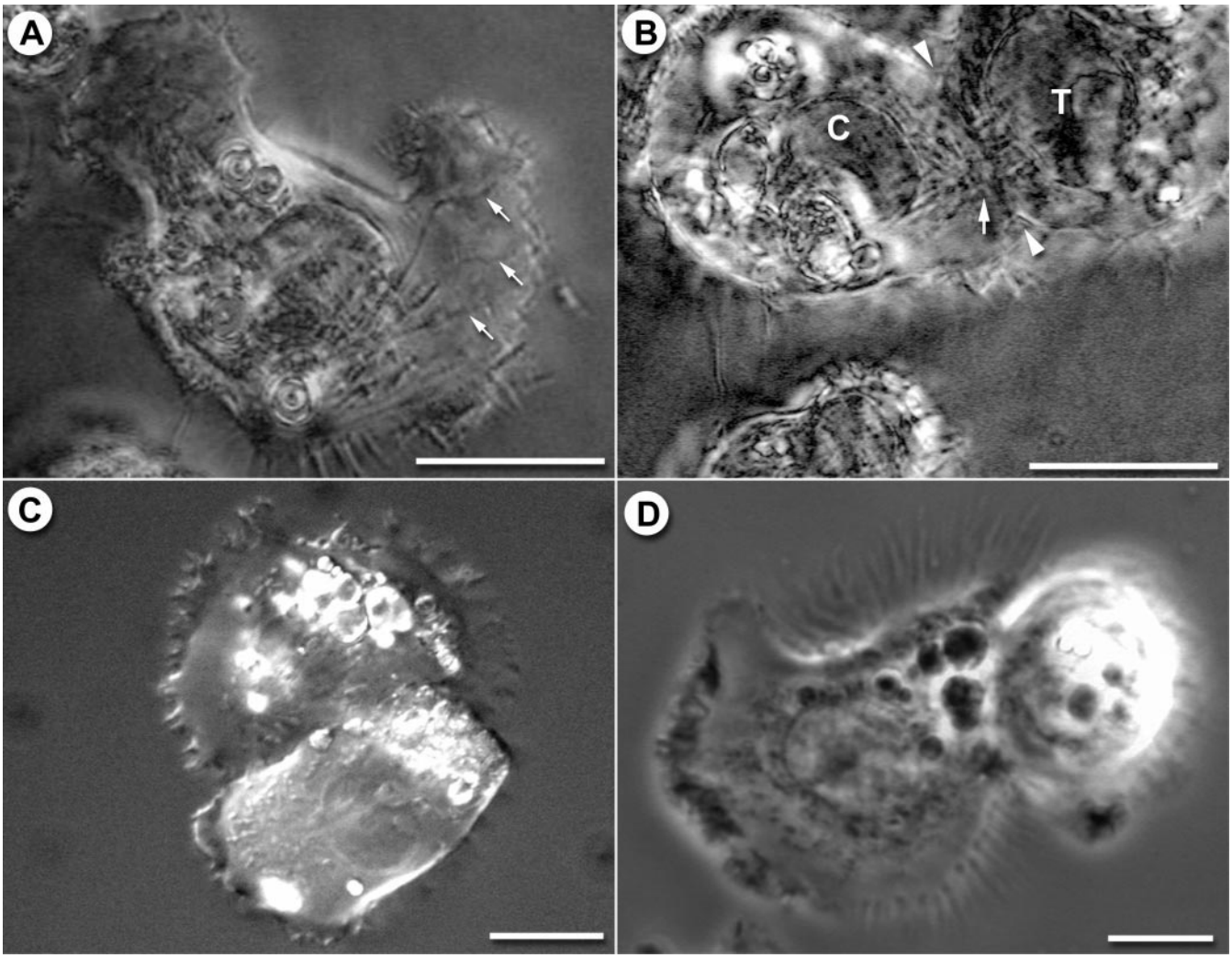

FIGURE 7 Cytotoxic T lymphocyte cytology by MPM, DIC, and phase contrast. (*A*) MPM image of a BM3.3 CTL shows structures resembling microtubules extending from a central point near the nucleus to the periphery of the cell (*arrows*). (*B*) MPM image of a CTL (*C*) bound to a target cell (*T*). The microtubule organizing center (*arrow*) can be seen under MPM to lie adjacent to the target contact site (between *arrowheads*). Representative DIC (*C*) and phase contrast (*D*) microscopy images of T lymphocytes are shown for comparison. *A–B* were obtained using an oil-immersion 1.4 NA 100× objective lens. *C* was obtained using an oil-immersion 1.4 NA 60× objective lens. Image *D* was obtained using an oil-immersion 1.3 NA 100× objective lens. Scale bars are 10 μm.

DISCUSSION

MPM represents a new approach to improving the contrast of weakly birefringent structures. Although there are other methods for improving contrast in polarized light microscopy, MPM is unique in its ability to accentuate birefringent elements while removing the background due to isotropic scatter. This is achieved by rotating the angle of polarization, which causes birefringent structures to vary in intensity while isotropic elements remain constant. As a result, much of the background is removed, allowing a much clearer picture of cytoskeletal elements and small vesicles.

The effectiveness of MPM depends in part on the ability to rotate the polarization angle of the illuminating light while retaining a crossed polarizer and analyzer configuration. In developing the microscope, a number of different approaches to rotating the angle of polarization were explored. These included Faraday rotators, liquid crystal rotators, Pockel cells, and simply rotating polarizer and analyzer in concert (Hartfield and Thompson, 1978). The main considerations were their suitability as imaging devices, which included the width of the acceptance angle and the degree to which polarization purity is maintained by the device in question. Pockel Cells were rejected based on their poor acceptance angle. Liquid crystal retarders were tried but they gave relatively poor polarization purity. We have also tried rotating half-wave plates, but our experience with wave plates accords with the experience of others in that it

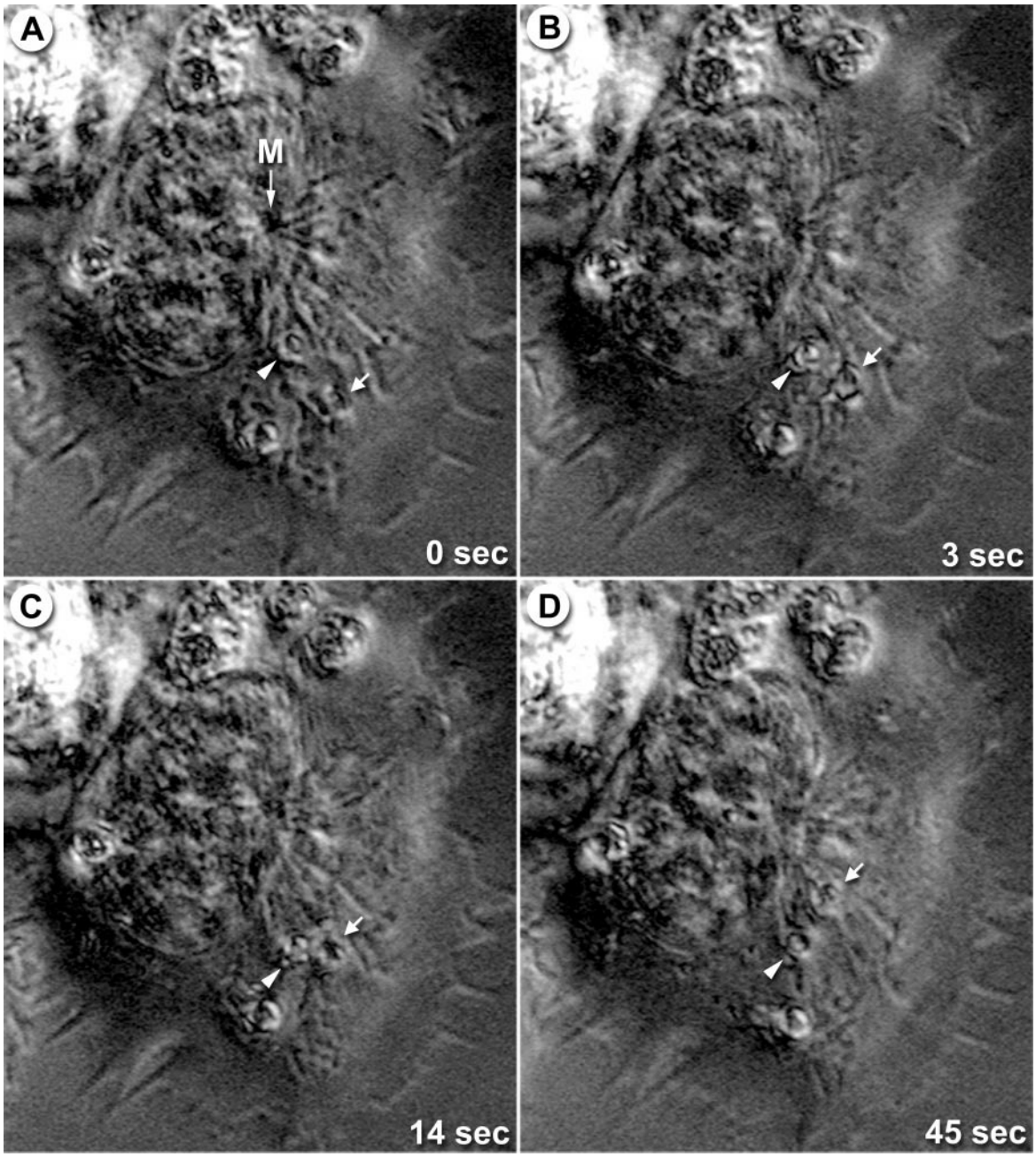

FIGURE 8 Detection of vesicle movements along microtubules in CTLs. Movement of vesicles along microtubules of CTLs is readily demonstrated in MPM images recorded over short time intervals as shown in *A–D*. In *A*, two different vesicles (one designated by an *arrow* and the other by an *arrowhead*) are associated with two different microtubules. At the outset, the vesicle designated by the arrowhead is closer to the nucleus and MTOC (*M*) than that designated by the arrow. As the sequence progresses, the vesicle designate by the arrowhead moves outward toward the cell periphery while the other vesicle moves inward toward the MTOC. *A–D* were obtained using an oil-immersion 1.4 NA 100× objective lens.

is difficult to obtain retarders that actually meet specifications (Goldstein and Chenault, 1997).

The choice of Faraday rotators was a compromise. Although they allow for high extinction values, they are expensive and they require large amounts of power (high magnetic fields), which greatly increases with diameter and they necessitate expanding the optical path. The expense and power requirements led to the choice of 2-cm-diameter rods. However, the lengthening of the optical path together with relatively narrow glass rods reduces the numerical aperture of the system to approximately 0.8. Although the problem could be largely alleviated with appropriate relay optics, these were initially avoided due to the increased depolarization additional lenses would add.

The large amount of power (400 Watts) dissipated by the Faraday rotator magnets requires that the magnets be water-cooled. As the temperatures of the glass rods increase, the amount of rotation obtained at a given magnetic field strength decreases. However, because rotation varies linearly with temperature over the operating range of the instrument, one can readily compensate for temperature effects by measuring the temperature of the magnets. In the prototype, we have used solenoid resistance as a measure of magnet temperature. Every two minutes, the MPM algorithm is stopped for three seconds while the magnet resistance is queried and the current values supplied to the magnets are updated. Between resistance measurements, the maximum rotation drops slightly from the ideal $\pm 45°$. Slight temperature differences between the two magnets leads to unequal rotation and an increase in the background. This can occasionally reverse the contrast between specimen and background (for examples, see Figs. 7 and 8). Modifications to the microscope underway include placing thermocouples inside of each solenoid that are continuously monitored by a data acquisition board. This permits temperature compensation between every MPM image.

The striking improvement in contrast obtained using MPM is readily evident when comparing images obtained between crossed polarizers without modulation to those obtained using MPM. In fact, MPM images often reveal filaments that are undetectable by conventional polarized light microscopy (for example, compare Fig. 3, *A* and *C*). However, filaments are not the only structures that show enhanced contrast and detail in MPM. Membrane-enclosed structures such as small vesicular elements are greatly enhanced in MPM. Thus with MPM one can identify both cytoskeletal fibers and vesicles that move along the fibers.

Although we can show that the stress fibers observed with MPM correspond to actin structures observed by fluorescent staining, we have not yet been able to do the same for microtubules. We have observed that both formaldehyde and gluteraldehyde fixation of cells changes the birefringence of their cytoplasm and significantly degrades the resulting MPM images. Although the birefringence of stress fibers is large enough to allow them to be seen with MPM in fixed cells, the birefringence of microtubules is much weaker, and they cannot be detected in fixed cells with MPM. We have also tried imaging CTLs that express GFP–tubulin both by fluorescence and MPM, but we were unable to obtain satisfactory images of microtubules by fluorescence on our MPM microscope. Thus, we have not yet formally proved that these structures are microtubules. For that, we would need another confirming method.

Despite these difficulties there are several reasons for concluding that the structures we observe by MPM in CTLs are in fact microtubules. (1) These structures are long contiguous filaments that are either straight or curved but never reticulated as with the endoplasmic reticulum. (2) They exhibit slow growth and rapid shortening typical of microtubules. (3) These filaments originate from a central point in the CTL that is always associated with the nucleus and they often take the form of a radial array of fibers. Furthermore, (4) nuclear movements in the CTL are always associated with the movement of these filaments. Finally, (5) one commonly observes vesicles tracking along these filaments as they move. Thus they exhibit all the properties that are characteristic of microtubules.

In the future, we anticipate that we will be able to observe microtubules in GFP–tubulin-expressing cells both by fluorescence and by MPM. We are currently in the process of converting the camera from an 8-bit analog CCD camera to a 12-bit, cooled digital camera. Using long integration times with the digital camera (3–5 s), we have obtained faint but clear fluorescent images of microtubules from CTLs that express GFP–tubulin, despite the large background fluorescence. However, obtaining a fluorescent image of the weak GFP signal requires slower acquisition times than with MPM, and the rapid bleaching of the GFP fluorophore limits the observation period to a few minutes of continuous data collection. Given the clarity of MPM images, rapidity of their acquisition, the capacity for long-term observation, and the ability of MPM to simultaneously observe microtubules and surrounding subcellular structure, MPM should provide a better avenue for studying the process of MTOC reorientation seen during CTL-mediated killing of target cells.

The lower noise and much greater gray-scale resolution of the digital camera should also greatly improve the MPM images. MPM is designed to extract weakly birefringent signals from a relatively large background. The performance of MPM is limited by noise, by the gray-scale resolution of the detector and by the loss of precision during data processing. The switch to a digital camera also entails using a host computer to process the images instead of the dedicated 8-bit image processing hardware that is used currently. The digital camera gives both a reduction in noise and great improvement in gray-scale resolution. Use of a host computer for image processing allows much greater precision because data is not restricted to 8 bits. Thus the use of a digital camera together with computer-based processing should give a large improvement in the quality of MPM images.

The current microscope can acquire MPM images at up to 2 Hz, and the images here are comparable to those at 1 Hz, even though only 16 polarization angles are captured. Unfortunately, the image-processing system is unable to save MPM images faster than two frames per second, so higher speeds and fewer polarization angles were not explored. It should be noted that the issue of speed involves not only the frame rate of the camera, but also camera noise. We suspect that the increase in noise seen at 2 Hz would become a serious limiting factor a higher speeds. In contrast, the power supplies have the ability oscillate at up to 1 KHz, and the system uses low-inductance, air-core magnets that

should accommodate fast current swings. With a low-noise, high-frame-rate digital camera, substantially faster MPM imaging should be possible.

In conclusion, MPM appears to be a promising step forward in polarized light microscopy. Even at this relatively crude stage of development, MPM reveals image details that are not evident by simple polarized light microscopy. Anticipated changes in the current prototype should yield significant improvements in image quality and structural detail.

This work was supported in part by a grant from the National Science Foundation (NSF) (DBI 9732131 award to M.P.) and an Advanced Technology Program grant from the Texas Higher Education Coordinating Board (003658-0355 awarded to M.P.).

Jeffrey Kuhn was supported in part, by a training grant, T32 GM 08368, from the National Institutes of Health.

We would like to thank Harris Semiconductor and Nova Marketing Inc. for donation of electronic parts and Nikon Instruments and Datacube for their participation NSF Presidential Young Investigator Award matching grants program.

REFERENCES

Allen, R. D. 1967. Optical differentiation of amoebic ectoplasm and endoplasmic flow. *Science.* 158:142–143.

Allen, R. D., and N. S. Allen. 1983. Video-enhanced microscopy with a computer frame memory. *J. Microsc.* 129:3–17.

Allen, R. D., J. Brault, and R. Moore. 1963. A New Method of Polarization Microscopic Analysis. *J. Cell Biol.* 18:223–235.

Allen, R. D., J. W. Brault, and R. M. Zeh. 1966. Image contrast and phase-modulated light methods in polarization and interference microscopy. *Adv. Opt. Electron Microsc.* 1:77–114.

Allen, R. D., and H. Nakajima. 1965. Two-exposure, film densitometric method measuring phase retardations due to weak birefringence in fibrillar or membranous cell constituents. *Exp. Cell Res.* 37:230–249.

Allen, R. D., and L. I. Rebhun. 1962. Photoelectric measurement of small fluctuating retardations in weakly birefringent, light-scattering biological objects. *Exp. Cell Res.* 29:583–592.

Azzam, R. M. A. 1978. Simulation of mechanical rotation by optical rotation: application to the design of a new Fourier photopolarimeter. *J. Opt. Soc. Am.* 68:518–521.

Baker, W. R., and J. A. Johnston. 1967. Optical differentiation of amoebic ectoplasm and endoplasmic flow. *Science.* 156:825–826.

Bennett, J. M. 1995. Polarizers. *In* Handbook of Optics, M. Bass, E. W. Van Stryland, D. R. Williams, and W. L. Wolf, editors. Vol. II. McGraw-Hill, Inc., New York. 3.1–3.70.

Cassimeris, L., S. Inoué, and E. D. Salmon. 1988. Microtubule dynamics in the chromosomal spindle fiber: analysis by fluorescence and high-resolution polarization microscopy. *Cell Motil. Cytoskeleton.* 10: 185–196.

Czaban, B. B., and A. Forer. 1985. The kinetic polarities of spindle microtubules *in vivo*, in crane-fly spermatocytes. *J. Cell Sci.* 79:1–65.

Farrar, J. J., J. Fuller-Farrar, P. S. Simon, M. L. Hilfiker, B. M. Stadler, and W. L. Farrar. 1980. Thymoma production of T cell growth factor (interleukin 2). *J. Immunol.* 125:2555–2558.

Geiger, B., D. Rosen, and G. Berke. 1982. Spatial relationships of microtubule-organizing centers and the contact area of cytotoxic T lymphocytes and target cells. *J. Cell Biol.* 95:137–143.

Gerdes, H. H., and C. Kaether. 1996. Green fluorescent protein: applications in cell biology. *FEBS Lett.* 389:44–47.

Goldstein, D. H., and D. B. Chenault. 1997. Evaluation of a selection of commercial polarizers and retarders at visible and near infrared wavelengths. *SPIE.* 3121:203–212.

Hansen, E. W. 1988. Overcoming polarization aberrations in microscopy. *SPIE.* 891:190–197.

Hartfield, E., and B. J. Thompson. 1978. Optical modulators. *In* Handbook of Optics. W. G. Driscoll, and W. Vaughan, editors. McGraw-Hill, New York. 17.1–17.24.

Inoué, S. 1981. Video image processing greatly enhances contrast, quality, and speed in polarization-based microscopy. *J. Cell Biol.* 89:346–356.

Inoué, S., and W. L. Hyde. 1957. Studies on depolarization of light at microscope lens surfaces. *J. Biophys. Biochem. Cyt.* 3:831–838.

Kupfer, A., and G. Dennert. 1984. Reorientation of the microtubule-organizing center and the Golgi apparatus in cloned cytotoxic lymphocytes triggered by binding to lysable target cells. *J. Immunol.* 133: 2762–2766.

Montgomery, D. B. 1980. Solenoid Magnet Design. R. E. Krieger, Huntington, NY.

Oldenbourg, R. 1996. A new view on polarization microscopy. *Nature.* 381:811–812.

Prendergast, F. G. 1999. Biophysics of the green fluorescent protein. *Methods Cell Biol.* 58:1–18.

Russell, J. H., and C. B. Dobos. 1983. Characterization of a "heteroclitic" cytotoxic lymphocyte clone: heterogeneity of receptors or signals? *J. Immunol.* 130:538–541.

Sitter, D. N., J. S. Goddard, and R. K. Ferrell. 1995. Method for the measurement of the modulation transfer function of sampled imaging systems from bar-target patterns. *Appl. Opt.* 34:746–751.

Swann, M. M., and J. M. Mitchison. 1950. Refinements in polarized light microscopy. *J. Exp. Biol.* 27:226–237.

Tsien, R. Y. 1998. The green fluorescent protein. *Annu. Rev. Biochem.* 67:509–544.

Wang, Y. L. 1989. Fluorescent analog cytochemistry: tracing functional protein components in living cells. *Methods Cell Biol.* 29:1–12.